Effect of Elastic Blade Deformation on Trim and Vibratory Loads of a Quadcopter

Robert Niemiec
Ph. D Student
Rensselaer Polytechnic Institute
Troy, NY, USA

Farhan Gandhi
Redfern Chair in Aerospace Engineering
Rensselaer Polytechnic Institute
Troy, NY, USA

ABSTRACT

This study examines the effect of rotor blade elastic deformations on a quadcopter in forward flight conditions. The blade equations are discretized using the Galerkin method and the blade periodic response is calculated using the harmonic balance method. Simulations are conducted on a 2 kg quadcopter with 12 inch diameter two-bladed rotors. The blade root vertical shear, flap bending moment and drag shear showed a strong 1/rev variation due to the azimuthal variation in aerodynamic loads. Elastic blade deformations did not affect the aerodynamic loads but the addition of in-phase 1/rev inertial loads resulted in net increases of 28%, 36% and 48% in the 1/rev blade root vertical shear, flap bending moment, and drag shear, respectively, at a forward flight speed of 10 m/s. The in-plane elastic deformations further introduced a 1/rev blade root radial shear due to the radial Coriolis force. At 10 m/s forward flight speed, accounting for elastic blade deformations resulted in a 7.6% reduction in the steady hub drag force, a 37% increase in steady hub roll moment, and a 15% increase in steady hub pitching moment that requires a 12% higher pitch RPM control input to trim the quadcopter. Increases of 103% in the 2/rev rotor hub in-plane loads (drag and side force), of 12% in the 2/rev hub vertical force, and of 25% in the 2/rev hub pitching and rolling moments were also observed. Since the forward rotor, lateral rotors, and the rear rotor operate at distinct rotational speeds, the aircraft is subject to vibratory loading at three different frequencies resulting in a beating phenomenon. The maximum amplitude of these oscillations equals the sum of the amplitudes of the three constituent vibrations, but reaches its maximum only once every twelve cycles. The 2/rev rotor hub vibratory moments are the dominant contributors to the aircraft pitch and roll vibrations, while the 2/rev rotor hub in-plane forces are the dominant contributors to the aircraft vibratory yaw moments. The blade phasing between the two lateral rotors has an effect on the magnitude of the total roll vibrations on the aircraft.

NOTATION

Ω	Rotor rotational velocity
R	Rotor Radius
A	Rotor Disk Area, πR^2
α_n^m, β_n^m	Peters-He dynamic inflow state
$\tau_n^{mc/s}$	Peters-He Modal Loads
Φ_n^m	Inflow modal function
ρ	Ambient air density
λ_i	Induced inflow ratio
x	Nondimensional radial location r/R
T	Axial tension
m	Mass per unit length
r	Dimensional radial location
u	Axial deformation, positive outboard
v	In-plane deflection, positive in lead
w	Out-of-plane deflection, positive up
E	Young's Modulus
$I_{z'}$	Second moment of area in flatwise direction
$I_{y'}$	Second moment of area in chordwise direction
θ	Local blade pitch relative to hub plane
$L_{v,w}$	Aerodynamic loading in lagwise and flapwise directions
M_ϕ	Aerodynamic torsional moment about blade sectional shear center
ϕ	Elastic shape function
$q_{v,w}$	Lag, flap Galerkin mode coefficient
$C_{S_{x,y,z}}$	Root drag, radial, and vertical shear coefficient
$C_{M_{x,y}}$	Root flapwise, torsional moment coefficient
$C_{h,Y,T}$	Hub drag, side force, thrust coefficient
C_0	Steady component of C
C_{ks}	kth harmonic sine component of C
C_{kc}	kth harmonic cosine component of C
ψ	Blade azimuth angle, 0° at rear of disk, increasing in direction of rotation

Presented at the AHS 73nd Annual Forum, Fort Worth, Texas, May 6–8, 2017.

INTRODUCTION

Multi-rotor helicopters are the subject of much interest among researchers and hobbyists, as well as in commercial applications, such as package delivery or aerial photography, or military applications like reconnaissance. Rather than use the cyclic pitch control of conventional helicopters, quadcopters use differential RPM on their rotors, which are used to generate the thrust and moments needed to control the aircraft.

Most often, the analysis of quadcopters is limited to simple rotor models, where the rotor thrust and torque are proportional to the square of the rotational velocity (Ω^2-model), with a proportionality constant that is invariant to the flight condition (Ref. 1). The Ω^2-model has proven sufficient to implement control strategies for a small-scale quadcopter (Ref. 2), even in the event of rotor failure (Ref. 3). More sophisticated rotor aerodynamic models are used by Bouabdallah and Siegwart (Ref. 4) and the authors (Ref. 5). Respectively, uniform inflow and a 3x4 Peters-He finite state dynamic wake (Ref. 6) were used to calculate rotor forces and moments via blade element theory. These studies all share the assumption that individual rotor blades are rigid.

Some other studies do not make the assumption of rigid rotor blades, modeling their elasticity as an articulated blade with a spring-restrained flapping hinge offset from the rotor axis. Rotor thrust is reoriented by the resulting tilt of the rotor tip-path plane, which is calculated in the steady state based on aerodynamic loads (Ref. 7), (Ref. 8), while the lag degree of freedom is not considered. Alternately, blade elasticity can be modeled using elastic beam theory under cyclic loading in a rotating reference frame. This study uses the equations of motion set forth by Hodges and Dowell in (Ref. 9) to model the elastic bending deformations in the flap and lag directions.

For a plus-type quadcopter considered in the present study, multi-rotor controls are used as outlined in (Ref. 10). These controls are defined as collective RPM control (Ω_0, Fig. 1(a)), roll control (Ω_R, Fig. 1(b)), pitch control (Ω_P, Fig. 1(c)), and yaw control (Ω_Y, Fig. 1(d)). The multirotor controls in Fig. 1 can be converted to individual rotor speeds via a linear transformation given by equation 1.

$$\begin{bmatrix} 1 & 0 & -1 & 1 \\ 1 & -1 & 0 & -1 \\ 1 & 0 & 1 & 1 \\ 1 & 1 & 0 & 1 \end{bmatrix} \begin{bmatrix} \Omega_0 \\ \Omega_R \\ \Omega_P \\ \Omega_Y \end{bmatrix} = \begin{bmatrix} \Omega_N \\ \Omega_W \\ \Omega_S \\ \Omega_E \end{bmatrix} \tag{1}$$

MODELING

Instantaneous rotor forces are calculated using Blade Element Theory; aerodynamic forces are evaluated on a differential section of each rotor blade, integrated over the span, and summed across all of the blades. In trim, the forces are averaged over a revolution. Inflow is modeled using the Peters-He finite-state dynamic wake model (Ref. 6) with 10 states for each rotor. Induced inflow dynamics are governed by the first-order ODE, Eq. 2. The induced inflow ratio itself is given as a function of (x, ψ), parameterized by the inflow states α_n^m and β_n^m in Eq. 3. The Peters-He model has two parameters, corresponding to the upper limits on m and n—the 10 state model used corresponds to $m_{max} = 3$, $n_{max} = 4$.

$$\begin{aligned} \Omega K \dot{\alpha}_n^m + V[L^c]^{(-1)} \alpha_n^m &= \frac{1}{2} \tau_n^{mc} \\ \Omega K \dot{\beta}_n^m + V[L^s]^{(-1)} \beta_n^m &= \frac{1}{2} \tau_n^{ms} \end{aligned} \tag{2}$$

$$\lambda_i(x,\psi,t) = \sum_{m=0}^{m_{max}} \sum_{n=m+1,m+3,\ldots}^{n_{max}} \Phi_n^m(x) \Big[\alpha_m^n(t) \cos(m\psi) + \beta_n^m(t) \sin(m\psi) \Big] \tag{3}$$

The elastic blade model uses the Hodges and Dowell equations of motion (Ref. 9), with torsion assumed to be zero, and the elastic axis assumed to be coincident with the tensile axis. The tensile axis is coincident to the locus of mass centroids because the blade section is homogeneous. The equations of motion are given by Eqs. 4–7. Equation 5 is the lag equation, and Eq. 6 is the flap equation. Airfoil section properties are calculated numerically about the area centroid, with a constant density of 1350 kg/m^3 and a Young's modulus of 8.273 GPa.

$$T' + m(\Omega^2 r + 2\Omega \dot{v}) = 0 \tag{4}$$

$$\begin{aligned} -(Tv')' + \Big\{ \Big(EI_{z'} \cos^2(\theta) + EI_{y'} \sin^2(\theta) \Big) v'' \\ + \Big(EI_{z'} - EI_{y'} \Big) \cos(\theta) \sin(\theta) w'' \Big\}'' \\ + 2m\Omega \dot{u} + m\ddot{v} - m\Omega^2 v = L_v \end{aligned} \tag{5}$$

$$\begin{aligned} -(Tw')' + \Big\{ \Big(EI_{z'} + EI_{y'} \Big) \cos(\theta) \sin(\theta) v'' \\ \Big(EI_{z'} \sin^2(\theta) + EI_{y'} \cos^2(\theta) \Big) w'' \Big\} \\ + m\ddot{w} = L_w \end{aligned} \tag{6}$$

$$T = EA \Big\{ u' + \frac{v'^2 + w'^2}{2} \Big\} \tag{7}$$

where $()' = d()/dr$ and $\dot{()} = d()/dt$. Equations 4 and 7 are used to eliminate T and u from the set of elastic equations, resulting in two dynamic equations in v (positive in lead) and w (positive upward).

The elastic equations are then reformulated into the weak form and a Galerkin method is used to solve the elastic deformation equations in terms of mode shapes (ϕ). The modes selected for out-of-plane and in-plane deformation are the same, and are chosen from the set of polynomials that satisfy the clamped-free boundary conditions, and are orthogonal to one another, with a tip displacement of 1. Mathematically,

$$\begin{aligned} \phi_i(0) &= 0 \qquad & \phi_i''(1) &= 0 \\ \phi_i'(0) &= 0 \qquad & \phi_i'''(1) &= 0 \\ \phi_i(1) &= 1 \\ \int_0^1 \phi_i(\xi) \phi_j(\xi) d\xi &= 0 \qquad i \neq j \end{aligned} \tag{8}$$

The first three modes are plotted in Fig. 2. The net displacement of a point on the rotor elastic axis is given by Eq. 9.

$$v(x,t) = \sum_{i=1}^{n} q_{v,i}(t)\phi_{v,i}(x)$$
$$w(x,t) = \sum_{i=1}^{n} q_{w,i}(t)\phi_{w,i}(x) \tag{9}$$

Where $q_{v,i}$ and $q_{w,i}$ are scalar functions of time.

In blade element theory, aerodynamic forces are evaluated on a differential section of the rotor blade. To do so, the incident velocities in the plane of the undeformed rotor are calculated (Eq. 10).

$$U_T = \Omega r + V_\infty \sin(\psi) + \dot{v}$$
$$U_P = \lambda_i \Omega r + V_c + \dot{w} \tag{10}$$

where U_T is the component of the velocity vector in the plane of the undeformed rotor (positive toward the trailing edge), and U_P is the component normal to the undeformed rotor plane (positive downward). The introduction of the $\dot{v}$ and $\dot{w}$ terms in Eq. 10 couple the aerodynamic forces to the elastic motion of the rotor. V_∞ and V_c are the in-plane and out-of-plane velocities of the rotor hub, respectively.

To estimate the steady rotor loads, the blade and inflow responses are assumed to be periodic in ψ, and a harmonic balance is used to calculate the coefficients. Upon convergence of the blade elastic and inflow response, aerodynamic forces are integrated along the span to obtain root shears (Eq. 11) and moments (Eq. 12), which are used to calculate discrete hub forces and moments. This is repeated for each rotor, and the rotor forces are added to external forces, such as gravity and fuselage drag, to determine the aircraft accelerations. These accelerations are used to update the trim controls, the rotor forces are reevaluated, until the trim controls converge to a state wherein the net accelerations are zero.

$$\text{Drag Shear} : S_x(\psi) = \int_0^R (-L_v(\psi) + m\ddot{v}(\psi))dr$$
$$\text{Radial Shear} : S_y(\psi) = \int_0^R (m\Omega^2 r + 2m\Omega\dot{v}(\psi))dr \tag{11}$$
$$\text{Vertical Shear} : S_z(\psi) = \int_0^R (L_w(\psi) - m\ddot{w}(\psi))dr$$

$$\text{Flapwise Moment} : M_x(\psi) = \int_0^R r(L_w(\psi) - m\ddot{w}(\psi))dr$$
$$\text{Torsional Moment} : M_y(\psi) = \int_0^R M_\phi(\psi)dr \tag{12}$$

To compare rotors that are not necessarily operating at the same rotor speed, the above shears and moments are normalized by $\rho A(\Omega R)^2$ and $\rho AR(\Omega R)^2$, respectively to yield force and moment coefficients. Similar treatment is given to the hub forces and moments.

The number of modes in flap and lag are varied throughout this study to determine how many modes are sufficient to capture the effects of elastic blade deformation on the predicted trim controls and the vibratory loads of the aircraft. Due to the nature of the rotor blade, flap and lag deformations are intrinsically coupled, so an equal number of modes for flap and lag are used in this study ("n modes" refers to "n modes in flap, and n modes in lag").

The simulation is based on the AeroQuad Cyclone ARF kit, which is a 2kg gross weight quadcopter with four 12-inch diameter rotors (Fig. 3). The rotor is assumed to be linearly tapered and twisted with properties listed in Table 1. The airfoil is a blend of the NACA4412 (at the root) and Clark Y (ai the tip).

Table 1. Aircraft Properties

Property	Value
Rotor Radius	0.1524m
Root Solidity	0.13
Tip Solidity	0.0514
Root Pitch	21.5°
Blade Twist	−10.4°
Young's Modulus	8.273 GPa
Blade Density	1350 kg/m^2
Boom Length	0.3048m
GTOW	2kg

TRIM RESULTS

For the front rotor of the quadcopter, Fig. 4 shows the tip out-of-plane and in-plane displacements of an individual blade as function of azimuth, at a high forward-speed condition of 10 m/s. The tip displacements shown are obtained using three Galerkin modes for both out-of-plane and in-plane deformations. Because the blade is highly twisted and lift and drag do not act along the principal axes, the out-of-plane and in-plane deflections are highly coupled. The lift, causing the blade to flap upward also causes it to lag backward. Thus, the lag response is seen to be in-phase with the out-of-plane response. Both the steady and the oscillatory components of the out-of-plane displacement are 2.9 times larger than the in-plane. Also shown on the figure is the aerodynamic lift integrated along the blade span. For the relatively stiff rotor on the quadcopter, the displacements are seen to be by-and-large in phase with the lift, which is substantially higher on the advancing side due to azimuthal variation in dynamic pressure and the absence of any cyclic pitch. Additionally, the aerodynamic drag (not shown) is also in phase with the lift.

Figure 5 shows the blade root shear forces (normalized by $\rho A(\Omega R)^2$) as a function of azimuth. Results are presented for

the case of a rigid blade as well as for an elastic blade (with increasing number of modes). From Fig. 5, while a single mode (1 flap, 1 lag) is seen to be insufficient, the root shears predicted using two modes (2 flap, 2 lag) are very close to those obtained with three modes (3 flap, 3 lag). A Fourier analysis of the root shear forces for both rigid and elastic blades is presented in Table 2. The blade root vertical shear (Fig. 5(c)) closely resembles the lift distribution in Fig. 4, and the blade root drag shear (Fig. 5(a)) is similarly driven by the aerodynamic drag. Both the vertical and drag shear show a dominant 1/rev sine component in their signals (also evident from the data in Table 2) due to the high dynamic pressure on the advancing side. Elastic deformations of the blade have negligible effects on the aerodynamic loads, but the inertial loads due to lead-lag accelerations are in phase with the aerodynamic drag and the out-of-plane inertial loads are similarly in phase with the lift. Consequently, the 1/rev blade root drag shear predictions with the elastic blade model are 48% higher than those with the rigid blade model (Fig. 5(a) and Table 2). For the 1/rev blade root vertical shear the elastic blade predictions exceed the rigid blade predictions by 28% (Fig. 5(c) and Table 2). With the rigid blade model, the blade root radial shear shows only a steady component due to the centrifugal force, and no oscillatory component. With the elastic blade model, however, an oscillatory component is observed as well (Fig. 5(b)). The oscillatory load is inertial in origin, attributed to the radial Coriolis force due to lead-lag motion. From Fig. 5(b), the radial shear shows a dominant 1/rev negative cosine component, but from both the figure as well as Table 2 it can be seen that other components are also present.

Table 2. Fourier Coefficients of Root Shear and Moment for Rigid and Elastic Blades

	0	1s	1c	2s	2c
	Rigid				
C_{S_x}	9.37e-4	5.06e-4	-6.91e-6	-6.68e-7	-5.90e-5
C_{S_y}	2.38e-1	0	0	0	0
C_{S_z}	4.35e-3	2.11e-3	-2.75e-4	-7.81e-5	-1.69e-4
C_{M_x}	4.67e-4	1.93e-4	-3.60e-5	-1.03e-5	-7.10e-6
C_{M_y}	2.61e-4	1.33e-4	-1.32e-5	-3.71e-6	-1.29e-5
	Elastic (2+ Modes)				
C_{S_x}	9.40e-4	7.43e-4	-6.99e-5	8.70e-5	-1.62e-5
C_{S_y}	2.38e-1	-7.16e-5	-2.74e-4	2.72e-5	-5.09e-5
C_{S_z}	4.36e-3	2.77e-3	-4.97e-4	1.90e-4	-6.10e-5
C_{M_x}	4.69e-4	2.61e-4	-6.07e-5	1.77e-5	4.63e-6
C_{M_y}	2.62e-4	1.34e-4	-1.55e-5	-2.20e-6	1.42e-5

Figures 6(a) and 6(b) show the blade root flap bending moment and the blade root torsion moment, respectively (both normalized by $\rho AR(\Omega R)^2$). The blade root flap bending moment (Fig. 6(a)) appears qualitatively very similar to the blade root vertical shear (Fig. 5(c)) as it originates from the same sources. Again, the difference between the rigid and elastic blade predictions are due to the inertial loads from blade flapping, which are in phase with the largely unchanged aerodynamic loads. The 1/rev blade root flap bending moments from the elastic blade model are 36% higher than the rigid blade predictions. With the aerodynamic center ahead of the elastic axis, there is a cyclic nose-up torsional moment associated with the generation of lift. The blade root torsion moment (Fig. 6(b)) is also maximum on the advancing side where the blade experiences the highest dynamic pressures and has a dominant 1/rev sine component to its signal. Any differences in blade root shears and blade root flapping moment between rigid and elastic blade predictions were attributed to inertial sources. Since torsional elasticity is not modeled, the rigid blade and elastic blade elastic results are very close (Fig. 6(b)). Harmonic components above 2/rev are small and not shown.

When moved from the rotating reference frame to the nonrotating hub frame, the 1/rev signals in blade root drag shear and radial shear, and the steady component of vertical shear produce steady forces, plotted in Fig. 7. Consider the effect of blade root drag and radial shear on the in-plane forces in the nonrotating frame, as well as the vertical shear on thrust.

$$\begin{aligned} \text{Thrust} : C_T(\psi) &= \sum_{i=1}^{n_{blades}} C^i_{S_z} \\ \text{Drag} : C_H(\psi) &= \sum_{i=1}^{n_{blades}} C^i_{S_x}\sin(\psi_i) + C^i_{S_y}\cos(\psi_i) \\ \text{Side Force} : C_Y(\psi_i) &= \sum_{i=1}^{n_{blades}} -C_{S_x}\cos(\psi_i) + C_{S_y}\sin(\psi_i) \end{aligned} \tag{13}$$

Expressing C_{S_x} and C_{S_y} as a Fourier series in Eq. 13 (Coefficients in Table 2) and summing over the two blades, it can be shown that the steady in-plane force coefficients on the rotor are

$$\begin{aligned} \text{Steady Thrust} : C_{T0} &= 2C_{S_z0} \\ \text{Steady Drag} : C_{H0} &= (C_{S_x1s} + C_{S_y1c}) \\ \text{Steady Side Force} : C_{Y0} &= (C_{S_y1s} - C_{S_x1c}) \end{aligned} \tag{14}$$

Because C_{S_x1s} is larger in magnitude than C_{S_y1c} (which is negative), the net drag is always in the direction of flow, as expected. Although C_{S_x1s} showed a large increase going from a rigid to elastic blade model, the negative change in C_{S_y1c} (due to radial Coriolis force) is even greater, to yield a 7.6% net reduction in drag at 10 m/s, as observed in Fig. 7(a), when elastic modes are used . The steady rotor hub side force (Fig. 7(b)) originates from the non-dominant components of the blade root radial and drag shear (C_{S_x1c} and C_{S_y1s}). Although the predicted side force shows changes between the rigid and elastic blade models, note that the magnitude of the side force is more than an order of magnitude smaller than the drag. Unlike the in-plane forces, only the steady component of blade root vertical shear contributes to the thrust coefficient (C_T, Fig. 7(c)). Because elastic motion does not affect the steady value of C_{S_z}, it does not affect the thrust coefficient.

The hub drag force coefficient is broken into aerodynamic and inertial components in Fig. 8. Because the displacements

are small (maximum tip deflection is 1% of the rotor radius), the effects that elasticity has on the aerodynamic forces are very small (Fig. 8(a)). Thus, all of the observed changes in C_H are due to inertial effects (shown in Fig. 8(b)).

Similar to the in-plane forces, 1/rev signals in the blade root flap bending moment and torsion moment produce steady hub rolling and pitching moments in the nonrotating frame.

$$\begin{aligned} \text{Steady Roll Moment} &: C_{L0} = (C_{M_x 1s} + C_{M_y 1c}) \\ \text{Steady Pitch Moment} &: C_{M0} = (C_{M_y 1s} - C_{M_x 1c}) \end{aligned} \tag{15}$$

Because both blade root flapping (C_{M_x}) and blade root torsion (C_{M_y}) are predominantly sine waves (Fig. 6), the former dominates in steady hub roll, while the latter dominates in steady hub pitch. Since the 1/rev blade root flapping moment (sine component) increased significantly with the use of the elastic deformation modes, a corresponding increase in hub rolling moment (37% at 10 m/s) is seen in Fig. 9(a). With the blade root torsion moment showing virtually no difference between the rigid and elastic blade models (Fig. 6(b)), all the observed difference in the hub pitching moment in Fig. 9(b) comes from changes in the 1/rev cosine component of the blade root flapping moment (C_{M_x}) going from the rigid to elastic blade model. This increase (seen in Table 2) results in a 15% increase in steady hub nose-up pitching moment at 10m/s (Fig. 9(b)). The steady hub torque coefficient (Fig. 9(c)) originating from the steady blade root lag moment is unaffected by the introduction of elasticity.

The modest reduction in the steady rotor hub drag causes a commensurate reduction in both the collective RPM (Fig. 10) and the quadcopter's pitch attitude (Fig. 11). The former is primarily driven by the thrust required to maintain altitude, and the latter by fuselage drag, so the observed changes to these controls is small. To counteract the additional nose-up pitching moment produced by the rotors when elasticity is included, a 12% increase pitch RPM is required at 10 m/s (Fig. 12). Although the steady roll moment coefficient experiences a large change, its direction is dependent on the rotor spin direction (a rotor spinning counter-clockwise produces a roll-left moment, while a rotor spinning clockwise produces a roll-right), so these moments counteract one another (with respect to the L^2 inner product), leaving the aircraft balanced in roll. Similarly, the side forces cancel.

VIBRATORY LOADS

To calculate the vibratory loads at the rotor hub, the blade root vibratory forces and moments (Figs. 5 and 6) must be summed over the number of blades as in Eq. 13. In the case of the hub loads of a two-bladed rotor every odd harmonic is cancelled. This cancellation is illustrated for the rotor thrust in Fig. 13. Although there is a strong 1/rev oscillation in individual blade root vertical shear, the total thrust has only a 2/rev oscillation superposed on the steady value. The vibratory loads can contain additional even harmonics, but as the frequency increases the amplitude of vibration tends to decrease. Any 4/rev vibratory loads were found to be negligible so the remainder of this study focuses on the 2/rev vibrations. From Eq. 13, the sine and cosine components of the 2/rev vertical and in-plane forces and the pitch and roll moments can be shown to be:

$$\begin{aligned} C_{H2s} &= C_{S_x 1c} + C_{S_y 1s} \\ C_{H2c} &= C_{S_x 1s} - C_{S_y 1c} \end{aligned} \tag{16}$$

$$\begin{aligned} C_{Y2s} &= -(C_{S_x 1s} - C_{S_y 1c}) \\ C_{Y2c} &= -(C_{S_x 1c} + C_{S_y 1s}) \end{aligned} \tag{17}$$

$$\begin{aligned} C_{T2s} &= 2C_{S_z 2s} \\ C_{T2c} &= 2C_{S_z 2c} \end{aligned} \tag{18}$$

$$\begin{aligned} C_{L2s} &= C_{M_x 1c} + C_{M_y 1s} \\ C_{L2c} &= C_{M_x 1s} - C_{M_y 1c} \end{aligned} \tag{19}$$

$$\begin{aligned} C_{M2s} &= -(C_{M_x 1s} - C_{M_y 1c}) \\ C_{M2c} &= -(C_{M_x 1c} + C_{M_y 1s}) \end{aligned} \tag{20}$$

From the above equations, it evident that the 2/rev vertical hub loads are generated from the 2/rev blade root vertical shear. The 2/rev hub drag and side force are generated only by the 1/rev blade root drag and radial shears (since the blade root drag and radial shear did not have any significant 3/rev content). In the absence of any 3/rev contributions to the vibratory in-plane forces, it is evident from Eqs. 16 and 17 that the amplitudes of the 2/rev hub drag and the 2/rev hub side force are identical. Similarly, the 2/rev hub pitch and roll moments originate from 1/rev blade root flap bending moment and torsion moment, and have identical magnitudes.

Figure 14 shows the 2/rev vibratory hub forces (normalized by $\rho A(\Omega R)^2$), and moments (normalized by $\rho AR(\Omega R)^2$) for the front rotor of the quadcopter at a forward speed of 10 m/s. On the elastic rotor, the magnitude of the 2/rev in-plane hub force (drag or side force) is 103% greater than that for the rigid rotor. Since the 1/rev blade root drag shear is predominantly a sine wave (Fig. 5(a), Table 2) and the 1/rev blade root radial shear is predominantly a (negative) cosine wave (Fig. 5(b), Table 2), from Eqs. 16 and 17, C_{H2c} and C_{Y2s} are the dominant contributors to the 2/rev hub drag and side-force, respectively. The large increase in 2/rev hub in-plane force going from the rigid to the elastic blade in Fig. 14(a) is due to the inertial loads being in-phase with the aerodynamic loads (Fig. 15(a)). Unlike the case of the steady hub drag, the Coriolis contribution from the radial shear and the inertial loads due to in-plane 1/rev lag vibrations are additive for the 2/rev hub loads.

For the 2/rev vertical hub force, the elastic blade predictions are only about 12% higher than the rigid blade predictions. Although the 2/rev inertial contributions are even larger than the aerodynamic contributions (the only source in the rigid blade case), Fig. 15(b) shows that the two are largely out-of-phase, resulting in only a small net increase in 2/rev vibratory hub force magnitude.

On Fig. 14(b), the 2/rev hub moment (pitch or roll moment) shows a 25% increase, going from the rigid to the elastic blade. The contributors to the pitch or roll moment are the 1/rev blade root flap bending moment and torsion moment (specifically the sine components dominate). Predictably, and as seen on Figs. 16(a) (for the rigid rotor) and 16(b) (for the elastic rotor), the flap bending moment and the torsion moment contributions are phased by 90°. The torsion moment remains unchanged between the rigid and elastic rotors. Although the magnitude of the flap bending moment increases by 36% going from the rigid to the elastic rotor, its contribution being out-of-phase with the torsion moment results in the more modest increase in 2/rev hub roll moment magnitude reported.

Rotor vibratory loads are transmitted directly to the airframe, with a frequency dependent on the individual rotor speed (Fig. 17). Because, in general, each of the four rotors on the quadcopter can operate at unique speeds, there are substantial vibrations at up to four frequencies (corresponding to the 2/rev on each rotor). At 10 m/s, the front-most rotor trims to a speed of 4560 RPM, while the lateral rotors and rear rotor trim to 5000 and 5380 RPM, respectively. This corresponds to 2/rev vibrations at 152.1 Hz, 165.4 Hz, and 179.3 Hz. Since the left and right rotors are operating at the same rotational speed in steady level flight, and assuming the rotors to be in-phase, their 2/rev vibrations add, resulting in the much hugher magnitude of vibratory loads on the aircraft at 165.4 Hz (Fig. 17). Comparing the front rotor's 2/rev contribution to the rear rotor's contribution in Fig. 17, the in-plane vibrations tend increase with rotor speed. However, the out-of-plane vibrations decrease with additional rotor speed. This is because the additional centrifugal stiffening of the rear rotor reduces its 2/rev out-of-plane deflection, and thus its inertial forces (2/rev aerodynamic loading is not as directly dependent on rotor speed).

Unlike in a conventional, single-rotor helicopter, the offset in frequency of the vibratory forces produces beats (shown in Fig. 18), with the overall amplitude of vibration varying over time. The overall in-plane vibrations are bounded by the sum of the individual amplitudes, but the system only reaches maximum vibratory loads approximately once for every twelve cycles an individual rotor experiences.

Moments are produced by the rotors at the aircraft level in two ways: transmission of hub moments to the airframe, and generation of forces at a distance from the aircraft reference point (taken to exist above the center of gravity in the shared hub plane). Hub pitching and rolling moments (Fig. 19), behave similarly to the drag and side-forces, with contributions from the left and right rotor summing to present a maximum-amplitude vibration. Additionally, the 2/rev variation in thrust on each rotor will result in a 2/rev oscillation in the rolling and pitching moment (Fig 20). For the lateral rotors, the roll moment from oscillatory thrust production behaves oppositely from their effect on thrust, i.e. when the rotors are phased by 90 degrees, the vibratory roll moments interfere constructively, and when they are in phase, the moments interfere destructively (Fig. 21). Similarly, these rotors' drag produces a vibratory yaw moment that behaves oppositely to the total drag with regard to the rotor phasing. This phasing, however, cannot be controlled (differential roll RPM may be required for disturbance rejection), so the vibrations presented are worst-case scenarios. Additionally, the front and aft rotor's thrust are incapable of producing a roll moment (as these rotors are on the roll axis), while the lateral rotors' thrust cannot produce a pitching moment. Side force on the front and rear rotors produces a yaw vibration in addition to that produced by the drag on the lateral rotors. Total vibratory moments (Fig. 22) are simply the vector sum of the vibrations due to hub moments and those due to hub forces. The aircraft vibratory pitch and roll moments are dominated by the hub moments, and the yaw moment is dominated by the vibratory in-plane rotor hub forces.

CONCLUSIONS

This study examines the effect of rotor blade elastic deformations on steady loads and trim, as well as the vibratory loads of a quadcopter in forward flight conditions. The equations of Hodges and Dowell are used to represent the blade in-plane and out-of-plane elastic bending deformations. The blade equations are discretized using the Galerkin method and the blade periodic response is calculated using the harmonic balance method. The aerodynamic loads are calculated using blade-element theory with the rotor induced velocities modeled using a 3x4 (10-state) Peters-He dynamic wake model. A coupled trim solution is obtained where convergence of both the blade response and vehicle equilibrium is satisfied. From the results in this study, the following conclusions were drawn:

The blade root vertical shear, flap bending moment and drag shear each showed a strong 1/rev variation originating from the azimuthal variation in aerodynamic loads in forward flight. Going from a rigid rotor to an elastic rotor, the aerodynamic loads showed little change, but 1/rev inertial loads due to blade flap and lag deformation, in-phase with the aerodynamic loads, resulted in net increases of 28%, 36% and 48% in the 1/rev blade root vertical shear, flap bending moment, and drag shear, respectively, at a forward flight speed of 10 m/s. Additionally, the in-plane elastic deformations resulted in a 1/rev blade root radial shear due to the radial Coriolis force (which was absent in the rigid blade model). The blade root torsional moment was not significantly affected by elastic bending.

Going from the rigid to the elastic blade, changes in the 1/rev signals in the blade root drag and radial shear produced a 7.6% reduction in the steady hub drag force at a forward

flight speed of 10 m/s. Similarly, changes in 1/rev blade root flapping moment produced a 37% increase in steady hub roll moment, and a 15% increase in steady hub pitching moment. While the roll moments cancel out at the aircraft level (with clockwise and counter-clockwise rotors producing roll moments in opposite directions), the nose-up pitching moments add, requiring a 12% greater pitch RPM control input at 10 m/s. The small reduction in steady hub drag mapped to a modest reduction in collective RPM and aircraft pitch attitude.

Going from the rigid to the elastic rotor resulted in significant increases in predicted 2/rev rotor hub vibratory loads. On the forward rotor, at 10 m/s forward slight speed, the largest increases (of 103%) were observed in the vibratory in-plane loads (drag and side force). The 2/rev rotor hub vertical force increased by 12%, while the 2/rev hub pitching and rolling moments were 25% larger.

Since the forward rotor, lateral rotors, and the rear rotor operate at distinct rotational speeds, the quadcopter experiences vibratory loading at three different frequencies. This results in a beating phenomenon, with a maximum amplitude of oscillations equal to the sum of the amplitudes of the three component oscillations, but reaches this maximum only once every twelve cycles. The aircraft vibratory pitch and roll moments (also at three frequencies) have contributions from the individual rotor hub moments as well as the thrust from the individual rotors. The 2/rev thrust from the front and aft rotors contribute to aircraft pitch vibrations at different frequencies (due to their different operational speeds) but the 2/rev thrust from the two lateral rotors contribute to the aircraft roll vibrations at the same frequency (since these rotors operate at the same speed in steady level flight). If the two lateral rotors operate in phase, the roll vibration from the thrust cancels but the roll vibration from the 2/rev hub moments add. The converse is true when the two lateral rotors are out of phase. In general, the aircraft pitch and roll vibrations are dominated by the vibratory hub moments (compared to the 2/rev vertical hub forces). The aircraft yaw vibrations are dominated by the 2/rev in-plane hub forces.

ACKNOWLEDGMENTS

This research was conducted with Government support under and awarded by DoD, Air Force Office of Scientific Research, National Defense Science and Engineering Graduate (NDSEG) Fellowship, 32 CFR 168a

REFERENCES

[1]Pounds, P., Mahony, R., Hynes, P., and Roberts, J. "Design of a Four-Rotor Aerial Robot," 2002 Australasian Conference on Robotics and Automation, Auckland, New Zealand, November 27–29, 2002.

[2]Mulgaonkar, Y., Cross, G., Kumar, V., "Design of Small, Safe, and Robust Quadrotor Swarms," 2015 IEEE International Conference on Robotics and Automation, Seattle, Washington, May 26-30, 2015.

[3]Mueller, M., D'Andrea, R., "Stability and Control of a Quadrocopter Despite the Complete Loss of One, Two, or Three Propellers," 2014 IEEE International Conference on Robotics and Automation, Hong Kong, China, May 31–June 7, 2014.

[4]Bouabdallah, S., and Seigwart, R., "Full Control of a Quadrotor," 2007 IEEE/RSJ International Conference on Intelligent Robots and Systems, San Diego, California, October 29–November 2, 2007.

[5]Niemiec, R., Gandhi, F., "Effects of Inflow Model on Simulated Aeromechanics of Quadrotor Helicopters" 72nd Annual Forum of the American Helicopter Society International, West Palm Beach, Florida, May 17–19 2016.

[6]Peters, D., Boyd, D., He, C., "Finite-State Induced-Flow Model for Rotors in Hover and Forward Flight," *Journal of the American Helicopter Society*, Vol. 34 (4), Oct. 1989, pp. 5-17. doi:10.4050/JAHS.34.5

[7]Pounds, P., Mahony, R., Gresham, J., Corke, P., and Roberts, J. "Towards Dynamically Favourable Quad-Rotor Aerial Robots," 2004 Australasian Conference on Robotics and Automation, Canberra, Australia, December 6–8, 2004.

[8]Hoffmann, G., Huang, H., Waslander, S., Tomlin, C., "Quadrotor Helicopter Flight Dynamics and Control: Theory and Experiment," AIAA Guidance, Navigation, and Control Conference and Exhibit, Hilton Head, South Carolina, August 20–23, 2007.

[9]Hodges, D., Dowell, E., "Nonlinear Equations of Motion for the Elastic Bending and Torsion of Twisted Nonuniform Rotor Blades," NASA TN D-7818, 1974.

[10]Niemiec, R., Gandhi, F., "Multi-rotor Coordinate Transforms for Orthogonal Primary and Redundant Control Modes for Regular Hexacopters and Octocopters," 42nd European Rotorcraft Forum, Lille, France, September 5–8, 2016.

FIGURES

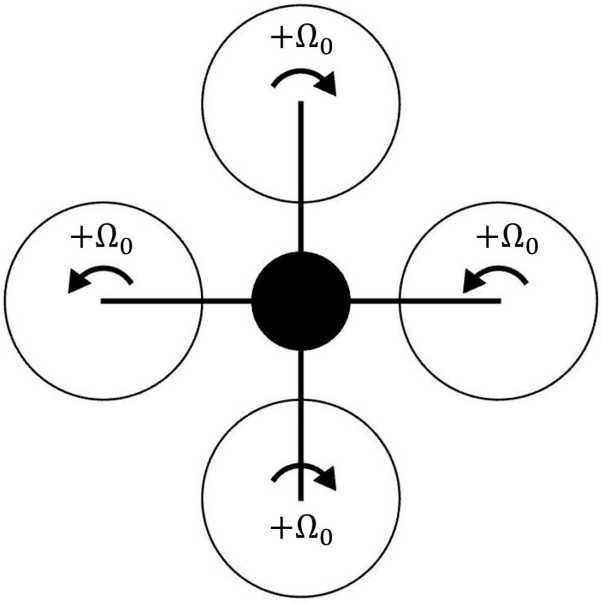

(a) Collective Control (Ω_0)

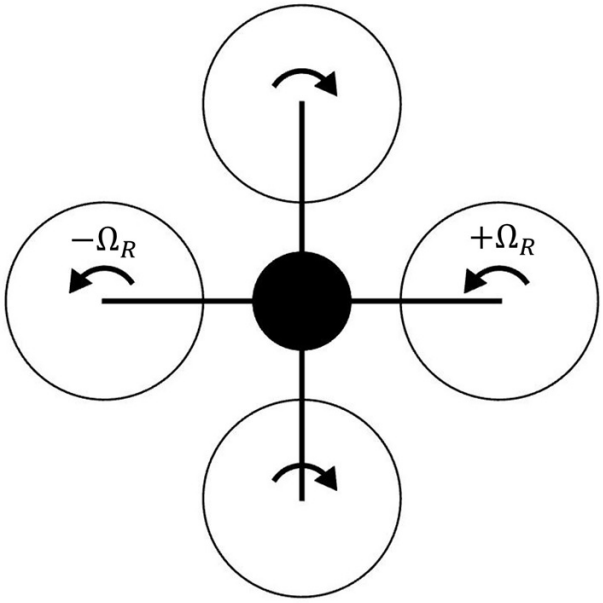

(b) Roll Control (Ω_R)

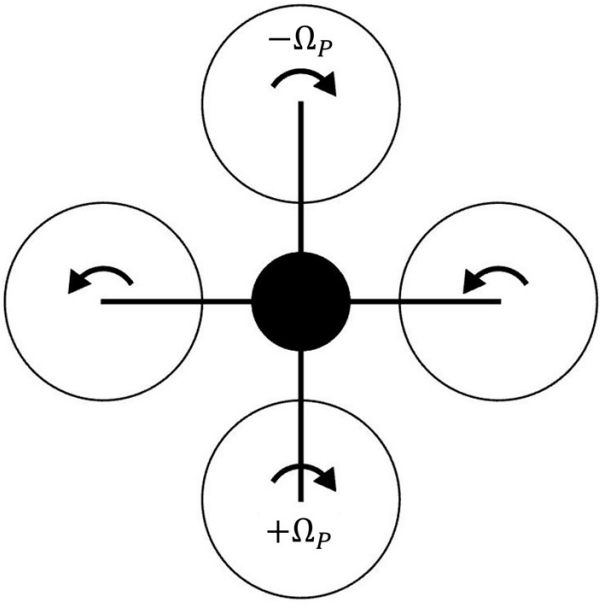

(c) Pitch Control (Ω_P)

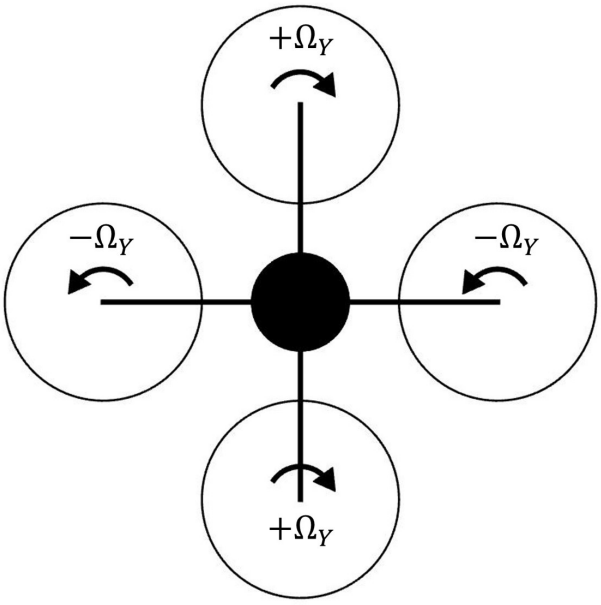

(d) Yaw Control (Ω_Y)

Fig. 1. Quadrotor multirotor controls

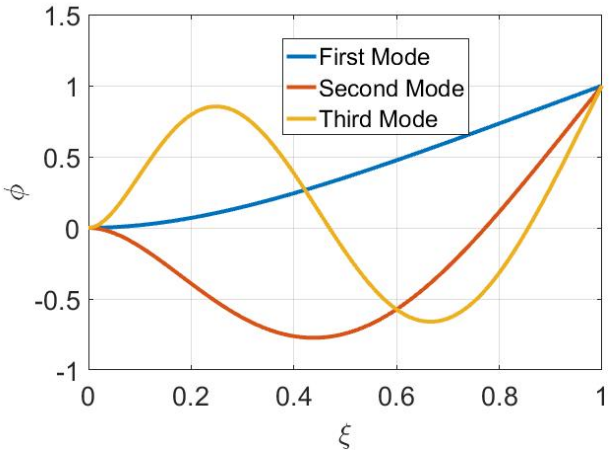

Fig. 2. Galerkin modes for elastic response

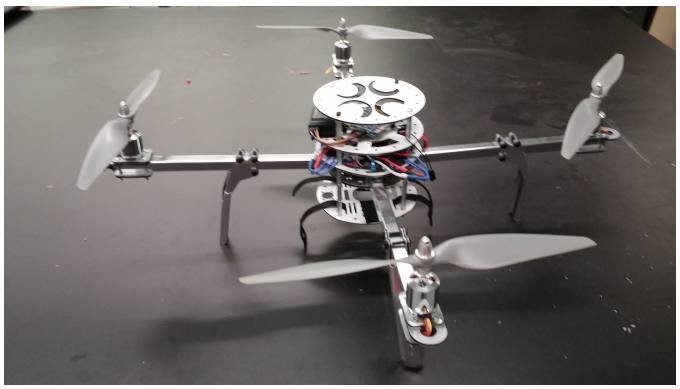

Fig. 3. AeroQuad Cyclone ARF Kit

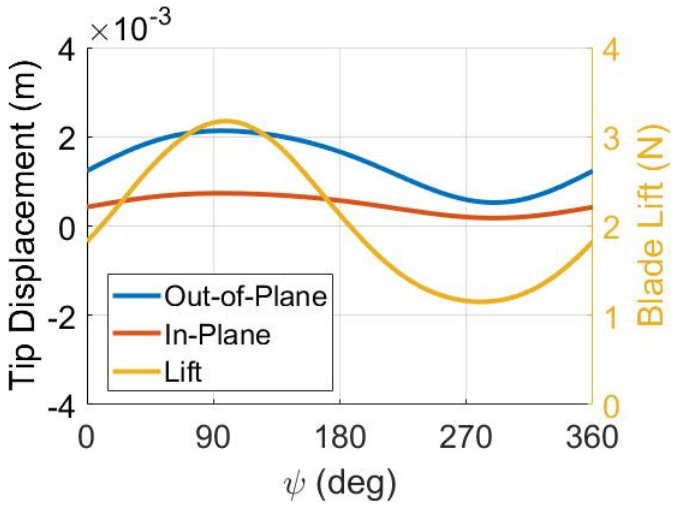

Fig. 4. Tip displacement of rotor blade on front rotor at 10 m/s (In-plane plotted as positive in lag)

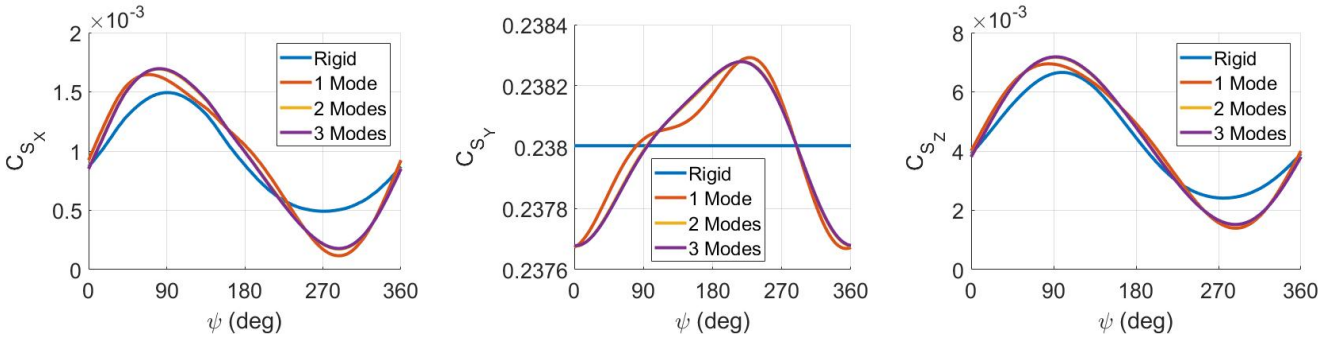

(a) x-shear (+ve toward trailing edge) (b) y-shear (+ve outboard) (c) z-shear (+ve up)

Fig. 5. Root shear loads on single blade on front rotor in 10 m/s forward flight (Normalized by $\rho A(\Omega R)^2$)

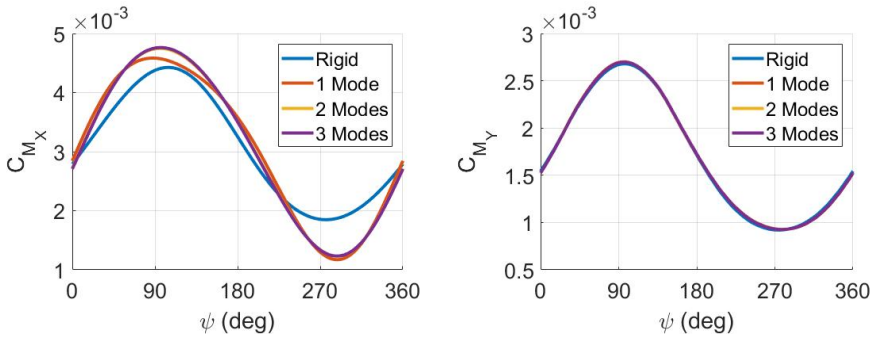

(a) Flap moment (+ve flap up) (b) Torsion Moment (+ve nose-up)

Fig. 6. Root bending moments on single blade on front rotor in 10 m/s forward flight (Normalized by $\rho AR(\Omega R)^2$)

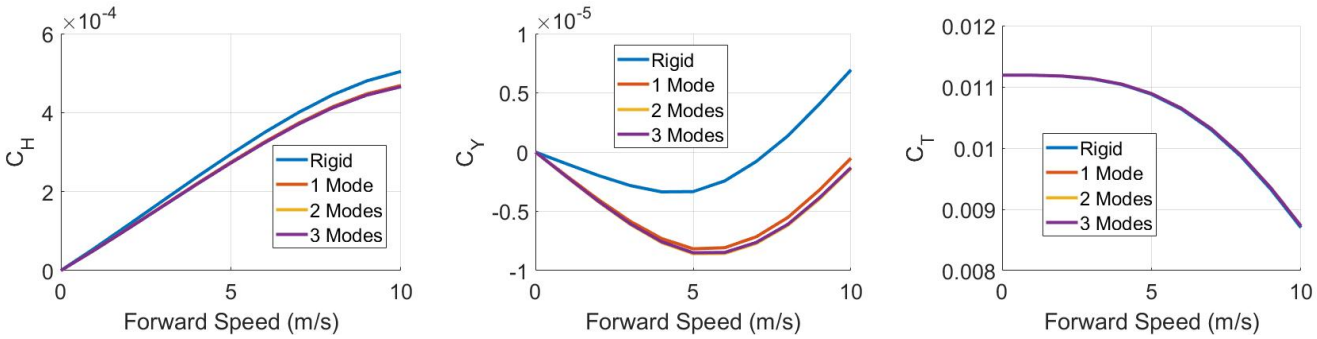

(a) H-Force Coefficient (b) Y-Force Coefficient (c) Thrust Coefficient

Fig. 7. Force coefficients for front rotor versus forward speed

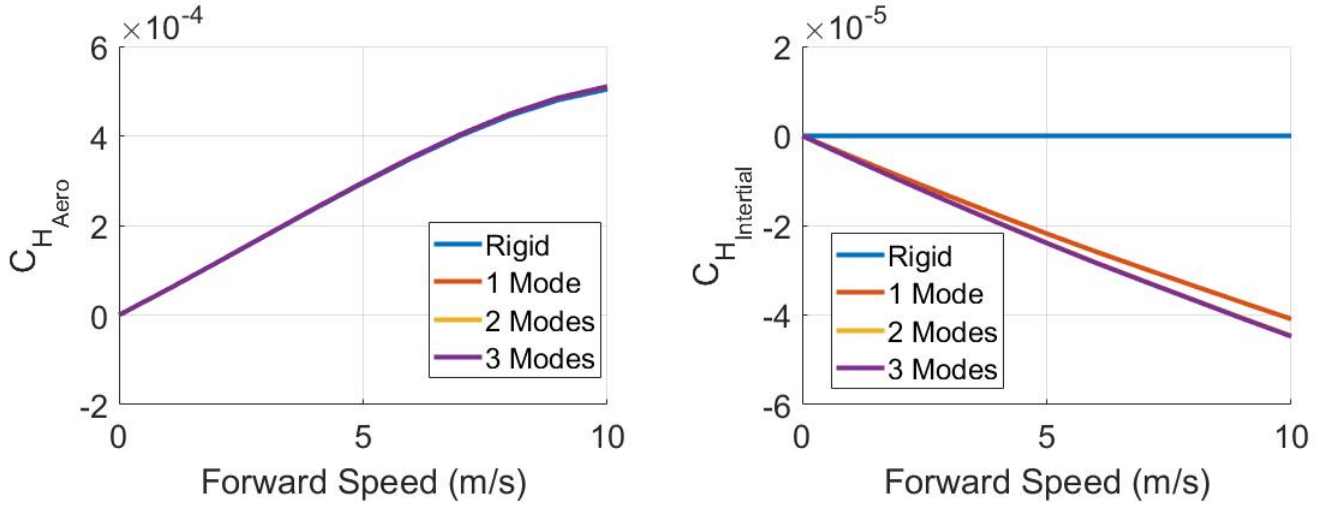

(a) Aerodynamic H-Force Coefficient (b) Inertial H-Force Coefficient

Fig. 8. Breakdown of H-Force on front rotor

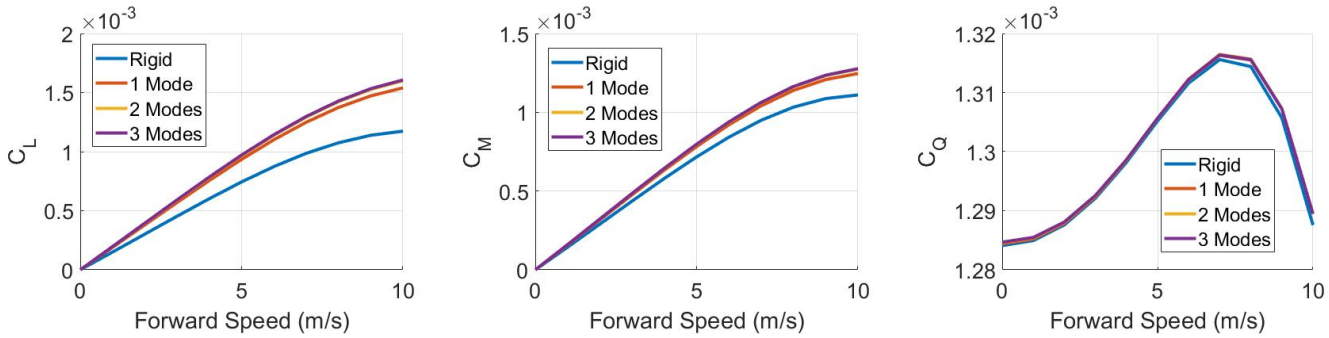

(a) Roll Moment Coefficient (b) Pitch Moment Coefficient (c) Torque Coefficient

Fig. 9. Moment coefficients for front rotor versus flight speed

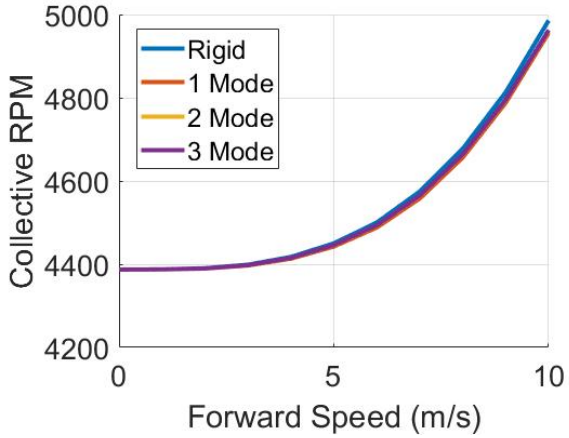

Fig. 10. Collective RPM control requirements versus speed

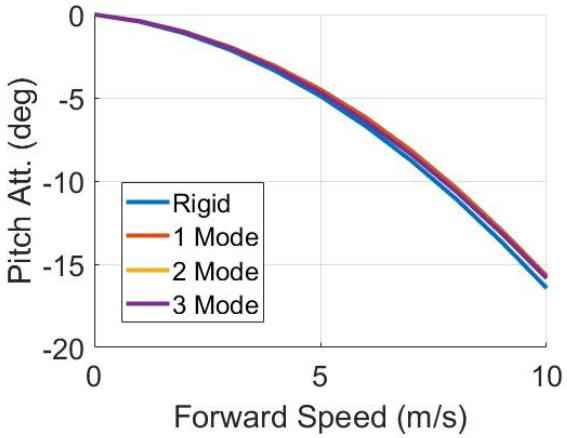

Fig. 11. Pitch attitude requirements versus speed

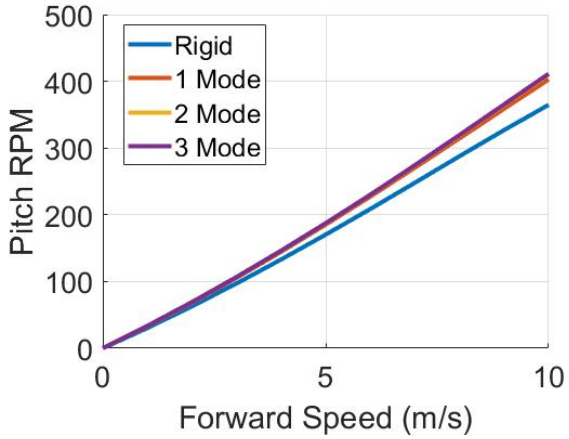

Fig. 12. Pitch control versus flight speed

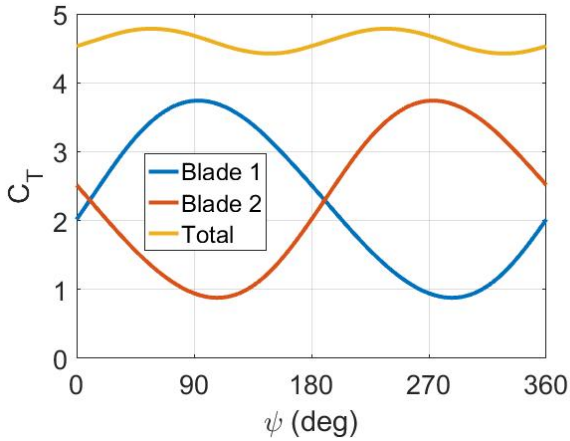

Fig. 13. C_T oscillation for front rotor at 10 m/s

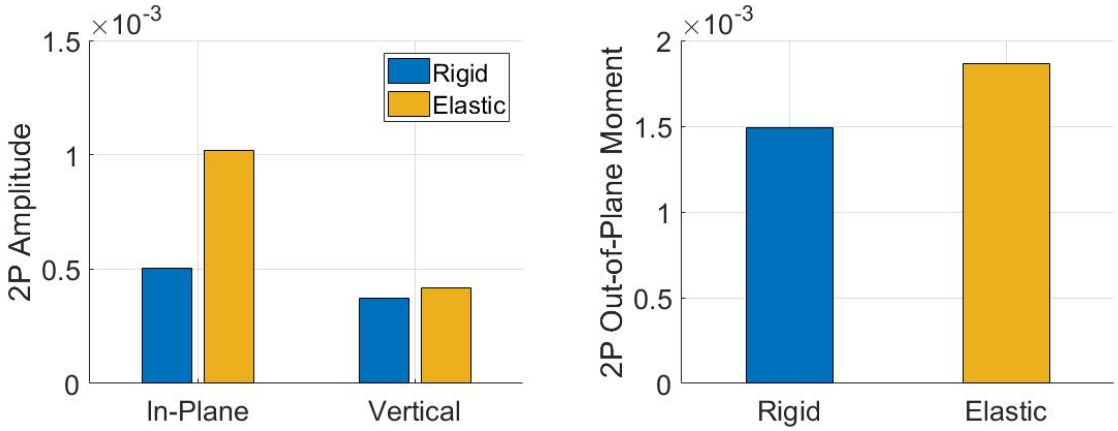

(a) Forces (Normalized by $\rho A(\Omega R)^2$) (b) Moments (Normalized by $\rho AR(\Omega R)^2$)

Fig. 14. 2P Force and moment oscillations on front rotor at 10 m/s

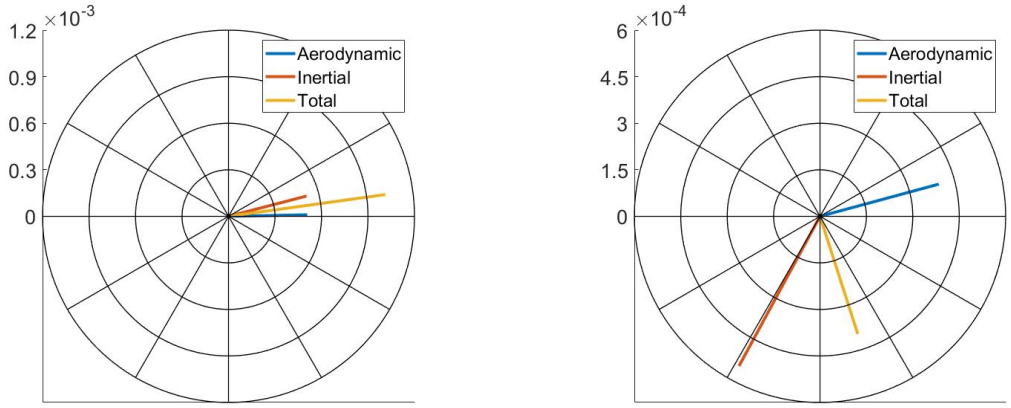

(a) In-plane (b) Out-of-plane

Fig. 15. 2P Vibratory forces on the front rotor at 10 m/s (normalized by $\rho A(\Omega R)^2$)

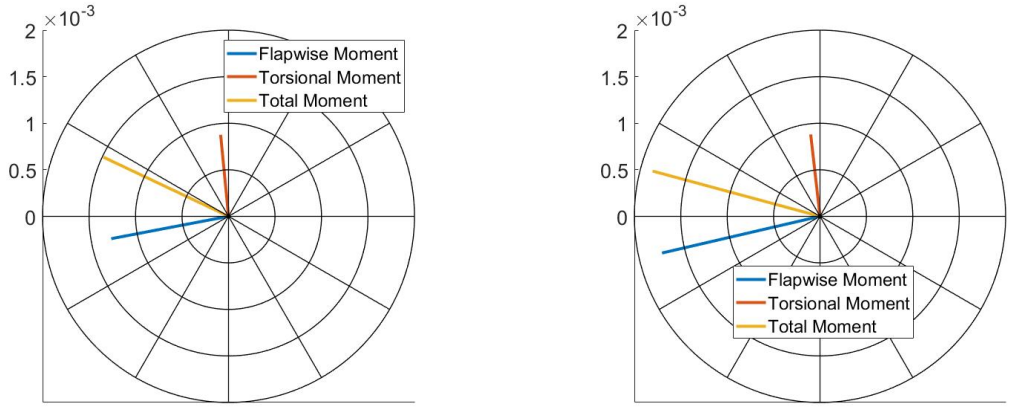

(a) Rigid (b) Elastic

Fig. 16. Amplitude and phase of hub roll moment sources on front rotor at 10 m/s (Normalized by $\rho AR(\Omega R)^2$)

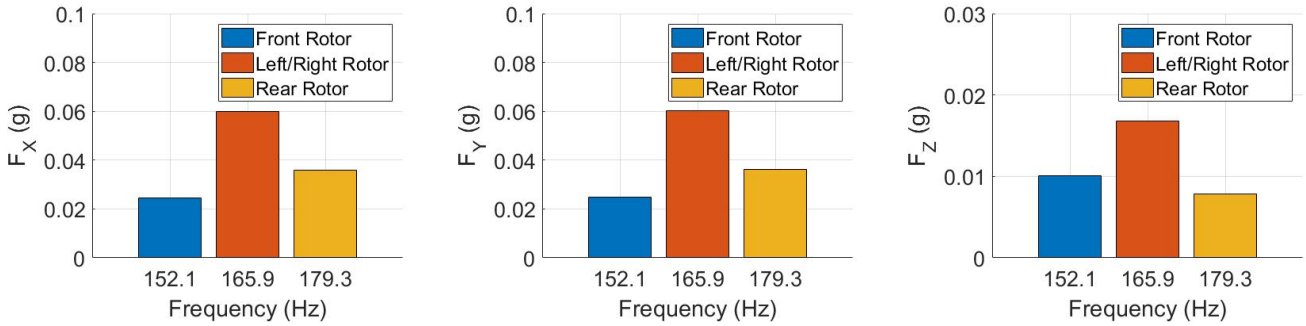

(a) Longitudinal vibration (b) Lateral vibration (c) Vetical vibration

Fig. 17. 2P vibratory forces on the aircraft at 10 m/s for elastic blade model

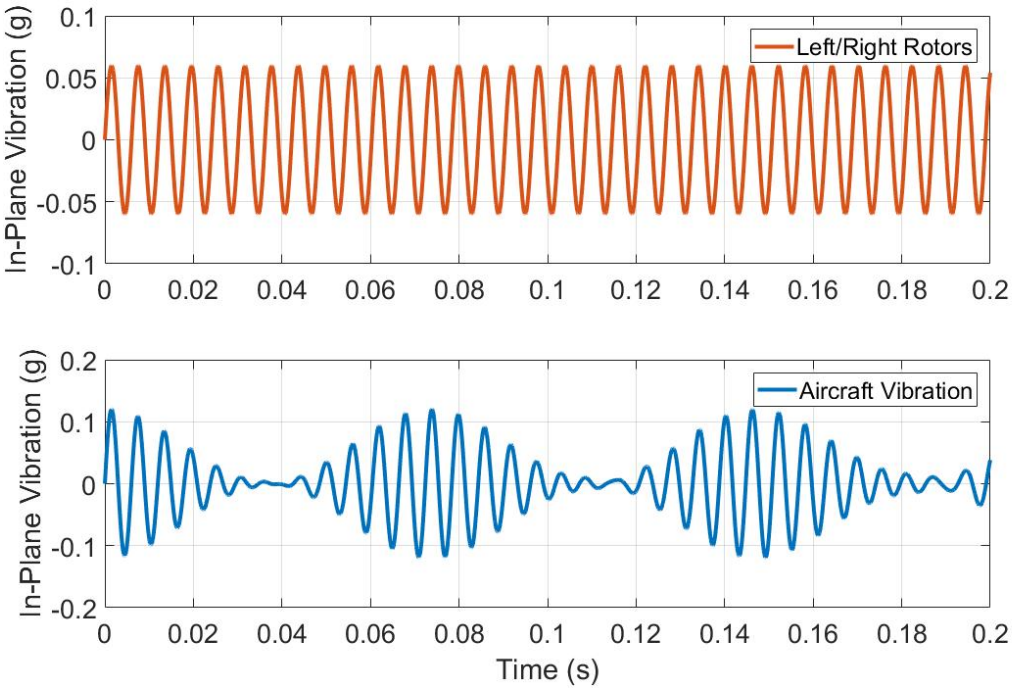

Fig. 18. Single rotor vibration (top) and total aircraft vibration (bottom)

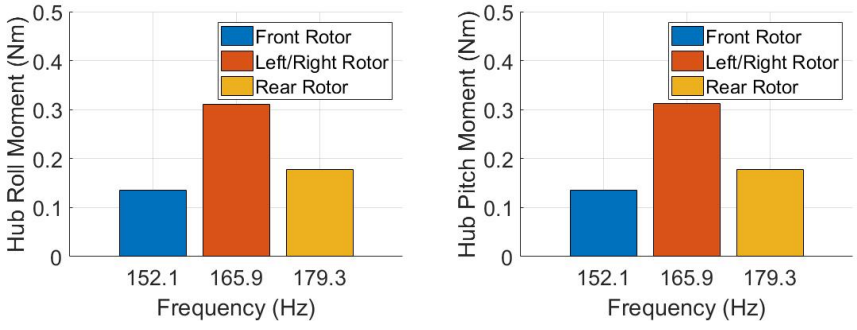

(a) Roll Vibration (b) Pitch Vibration

Fig. 19. Aircraft Vibratory Moments from Hub Moments at 10 m/s

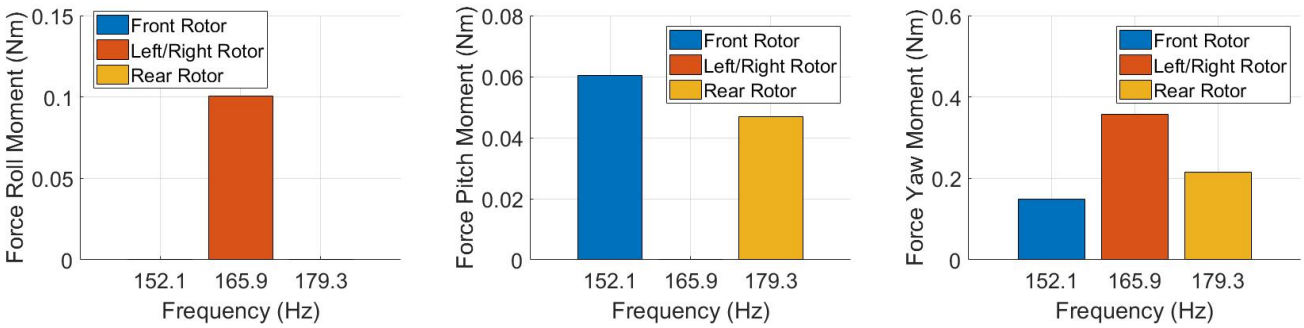

(a) Roll Vibration (b) Pitch Vibration (c) Yaw Vibration

Fig. 20. Aircraft Vibratory Moments from Hub Forces at 10 m/s

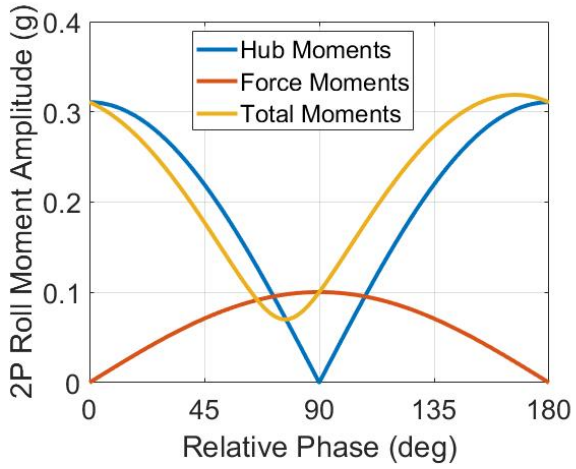

Fig. 21. Amplitude of aircraft roll moment vibration at 165.4 Hz versus phase angle between left and right rotors at 10 m/s for the elastic rotor

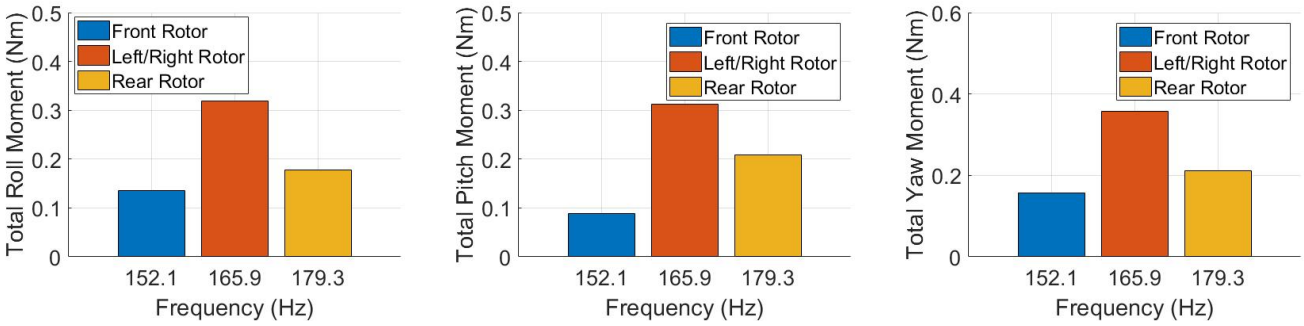

(a) Roll Vibration (b) Pitch Vibration (c) Yaw Vibration

Fig. 22. Total Aircraft Vibratory Moments at 10 m/s